ADVANCED OPTICAL MATERIALS
www.advopticalmat.de

Strategies to Control Crystal Growth of Highly Ordered Rubrene Thin Films for Application in Organic Photodetectors

Anna-Lena Hofmann, Jakob Wolansky, Mike Hambsch, Felix Talnack, Eva Bittrich, Lucy Winkler, Max Herzog, Tianyi Zhang, Tobias Antrack, L. Conrad Winkler, Jonas Schröder, Moritz Riede, Stefan C.B. Mannsfeld, Johannes Benduhn,* and Karl Leo**

Organic semiconductors still lag behind their inorganic counterparts in terms of mobility due to their lower structural order, in particular in thin films. Here, the highly ordered phase of triclinic rubrene – characterized by high vertical hole mobility – grown from a vacuum-deposited thin film is used by post-annealing and implemented into organic photodetectors. Since the triclinic rubrene exhibits a high roughness with a peak-to-valley value of 250 nm, which is detrimental to the dark current, strategies to control the crystal growth are developed. These investigations show that a suppression layer of 20 nm C_{60} is the most promising approach to successfully reduce the surface roughness while maintaining the triclinic phase, proven by grazing-incidence wide-angle X-ray scattering (GIWAXS). With the smoothened active layer, the dark current density is reduced by three orders of magnitude compared to the neat rubrene layer. It is as low as 2.5 × 10^{-10} A cm^{-2} at −0.1 V bias, reflected in an overall specific detectivity of 6 × 10^{11} Jones at zero bias (based on noise measurements) and a high linear dynamic range of 170 dB. This strategy using a suppression layer thus proves successful and is very promising to be applied to other crystalline materials.

1. Introduction

Due to their manifold applications, photodetectors (PDs) have a rapidly growing market. They have become indispensable in environmental monitoring, medical imaging, and optical communication.[1,2] PDs are no longer only used by research or industry but have also found their way into the private sector, particularly in wearables, whose popularity is being fuelled by ever smaller and cheaper devices.

Although the widely used crystalline inorganic semiconductor PDs, mainly silicon and indium-gallium-arsenide, perform well, they require clean-room manufacturing, are energy-intensive to produce, and their bulky nature makes integration into flexible devices challenging.[3] In contrast, PDs based on organic semiconductors offer mechanical flexibility and low-cost production. Moreover, they allow wide spectral tunability, transparency, biocompatibility, and deposition onto almost any substrate given by their low-temperature deposition processes.[4,5] These possibilities stimulated intense research in recent years, tremendously improving the performance of organic photodetectors (OPDs). In terms of specific detectivity D^*, record values above 10^{14} Jones have been reached for a blue OPD, more than one order of magnitude higher than commercial silicon photodiodes in the same spectral range.[6,7]

A.-L. Hofmann, J. Wolansky, L. Winkler, M. Herzog, T. Zhang, T. Antrack, L. C. Winkler, J. Schröder, J. Benduhn, K. Leo
Dresden Integrated Center for Applied Physics and Photonic Materials (IAPP) and Institute of Applied Physics
Technische Universität Dresden
Nöthnitzer Str. 61, 01187 Dresden, Germany
E-mail: anna-lena.hofmann@tu-dresden.de; johannes.benduhn@tu-dresden.de; karl.leo@tu-dresden.de

The ORCID identification number(s) for the author(s) of this article can be found under https://doi.org/10.1002/adom.202401025

DOI: 10.1002/adom.202401025

M. Hambsch, F. Talnack, S. C. Mannsfeld
Center for Advancing Electronics Dresden (cfaed) and Faculty of Electrical and Computer Engineering
Technische Universität Dresden
Helmholtzstr. 18, 01069 Dresden, Germany

E. Bittrich
Leibniz-Institut für Polymerforschung Dresden e.V.
Institute of Macromolecular Chemistry
Hohe Str. 6, 01069 Dresden, Germany

M. Riede
Department of Physics
University of Oxford
Parks Road, Oxford OX1 3PU, UK

Beyond that, a broad range of OPDs reach D^* values in the order of 10^{13} Jones and a linear dynamic range (*LDR*) between 100 and 200 dB.[8,9] These characteristics emphasize that OPDs can compete with or even outperform current commercial PDs. However, key parameters like the dark current density J_d strongly depend on the selected active layer and charge blocking layers. For systems based on C_{60}, J_d ranges, e.g., from 10^{-8} to 10^{-12} A cm^{-2} at −0.1 V.[6,10,11] Since the dark current usually limits the detectivity, a better understanding is essential for achieving an even better performance.

For applications in optical communication, a high response speed is required. While inorganic PDs already reach response speeds in the GHz regime, OPDs are, in most cases, still limited to the kHz and lower MHz regime.[8,12,13] With the concept of balanced hole and electron extraction times, a cutoff frequency of 68 MHz could be achieved for a ZnPc-C_{60} system by Ullbrich et al.[14] Zheng et al. achieved an even higher bandwidth of 107 MHz with a simple TAPC-C_{70} planar heterojunction and justified this with comparable high mobilities of both materials in the order of 10^{-2} cm^2 V^{-1} s^{-1}.[15] The charge mobility is crucial for optimizing OPDs to a high response speed and, additionally, a low *RC* value (with *R* as series resistance and *C* as the device's capacitance) is a necessary prerequisite. However, amorphous small molecule organic semiconductors typically exhibit mobilities in the range of only 10^{-5} to 10^{-2} cm^2 V^{-1} s^{-1}.[16–18] The main limiting factor for such low mobilities is the disordered nature of the amorphous organic semiconductors, leading to localized charge carriers and thermally activated hopping as the major transport mechanism.

The latter can be addressed by a high molecular order present in organic crystals. Out of the many synthesized organic molecules, only a few can be grown as single crystals. Based on benzene rings, anthracene, tetracene, pentacene, TCNQ, and rubrene (5,6,11,12-Tetraphenyltetracen) are prominent examples. Moreover, systems like BPTTE and tetra[2,3]thienylene tetracarboxylic acid based on thiophene units are able to form crystals, too.[19,20] Some molecules can be crystallized only from solution, whereas other molecules can be grown into a crystal by physical vapor deposition or even both methods. While anthracene, tetracene, and TCNQ exhibit moderate mobilities in the order of 1 cm^2 V^{-1} s^{-1}, BPTTE reaches 18 cm^2 V^{-1} s^{-1}, pentacene 35 cm^2 V^{-1} s^{-1}, and rubrene even a record high value of 40 cm^2 V^{-1} s^{-1} at room temperature.[19,21–25] The values have been obtained mostly from field-effect transistor structures, where the mobilities are usually higher than in diode structures. Nevertheless, high values of 10 cm^2 V^{-1} s^{-1} have been achieved for a diode architecture with triclinic rubrene.[26]

Apart from their high mobility, single crystals are difficult to handle and primarily restricted to lateral devices, like organic field effect transistors (OFETs) or phototransistors.[27–30] Moreover, single crystals require a high temperature for growth or need to be grown from solution.[20,31] However, thin films are more viable for many different applications and are compatible with vertical structures, e.g. diodes, as several layers can be sequentially stacked on top of each other. Also, they can be prepared on almost any substrate and be upscaled to large-scale industrial processes. Among the above-mentioned materials, the most favorable material for crystalline thin films is rubrene. Besides its high hole mobility, it absorbs in the visible range, which makes it a promising candidate for fast vertical OPDs.

The crystallization of rubrene thin films was first observed accidentally by Park et al., where crystalline disks appeared after the evaporation.[32] To control the crystallization, rapid heating of the previously amorphous film is applied.[33] Thus, the choice of the crystalline phase of rubrene thin films, which are triclinic or orthorhombic, can be precisely adjusted via the annealing temperature.[34] The monoclinic phase, another crystalline phase of rubrene, can only be observed for solution-grown crystals.[35] For good crystal quality, the crystallization process should take place in an inert and dark environment.[33,36] This is challenging for methods like inkjet printing, but easily possible by physical vapor deposition. The initial, annealed layer is usually several tens of nanometers thick. With homoepitaxy, the layer thickness can be increased significantly while preserving crystallinity. The concept of homoepitaxy has been successfully applied to organic light-emitting diodes (OLEDs), for example, in which more than 500 nm of triclinic rubrene is grown on a 50 nm thick microcrystalline layer.[6] Furthermore, it has been shown that these crystalline stacks can also be *p*- and *n*-type doped, allowing devices such as pin-diodes[26] and bipolar transistors.[37]

Depending on the crystalline phase, the distance and the direction of the nearest molecule along the backbone stacking differs. For the triclinic phase the π-stacking is along the *a*-axis (7.02 Å)[35] as shown in the crystal structure in **Figure 1d**.[34] Given the polycrystalline nature of our thin film, achieving a precise determination of the unit cell's orientation concerning the substrate proves elusive. However, it is possible to observe a preferential orientation of the neat triclinic rubrene film to the substrate in the scanning electron microscopy (SEM) image in Figure S2b (Supporting Information). Even though the symmetry and the expected mobility are generally higher for the orthorhombic phase, the triclinic phase exhibits hole mobilities as high as 10 cm^2 V^{-1} s^{-1} in the vertical direction.[26] Therefore, the triclinic phase proves more suitable, especially in the vertical direction compared to the orthorhombic phase, where values of only 2 cm^2 V^{-1} s^{-1} have been measured.[38] Since our goal is to fabricate vertical OPDs, we utilize the triclinic rubrene phase as the active layer. To overcome the challenge of high dark currents, which have a detrimental effect on the overall OPD performance, we identify the increased surface roughness of triclinic rubrene, causing Ohmic shunts, as the crucial reason these samples fall short in the specific detectivity. Therefore, we implement several strategies to smoothen the surface of the active layer, while the crystalline nature of rubrene is maintained. Different epitaxially grown active layers are investigated. When co-evaporating the rubrene layer with 5 wt.% of C_{60} on top of the triclinic seed layer, the improvement is only minor, whereas an active layer with C_{60} doped by 6 wt.% of rubrene reduces the dark current by one order of magnitude. Likewise, the addition of a C_{60} layer on top of the crystalline neat rubrene film reduces the dark current by one order of magnitude. However, the most promising approach is establishing a suppression layer (suppressing the film surface roughness) which is evaporated on top of the rubrene layer before annealing the sample at 140 °C. Compared to the neat rubrene layer, we can thereby minimize the dark current by three orders of magnitude. After optimizing the electron transport layer in terms of material and thickness, we finally achieve a dark

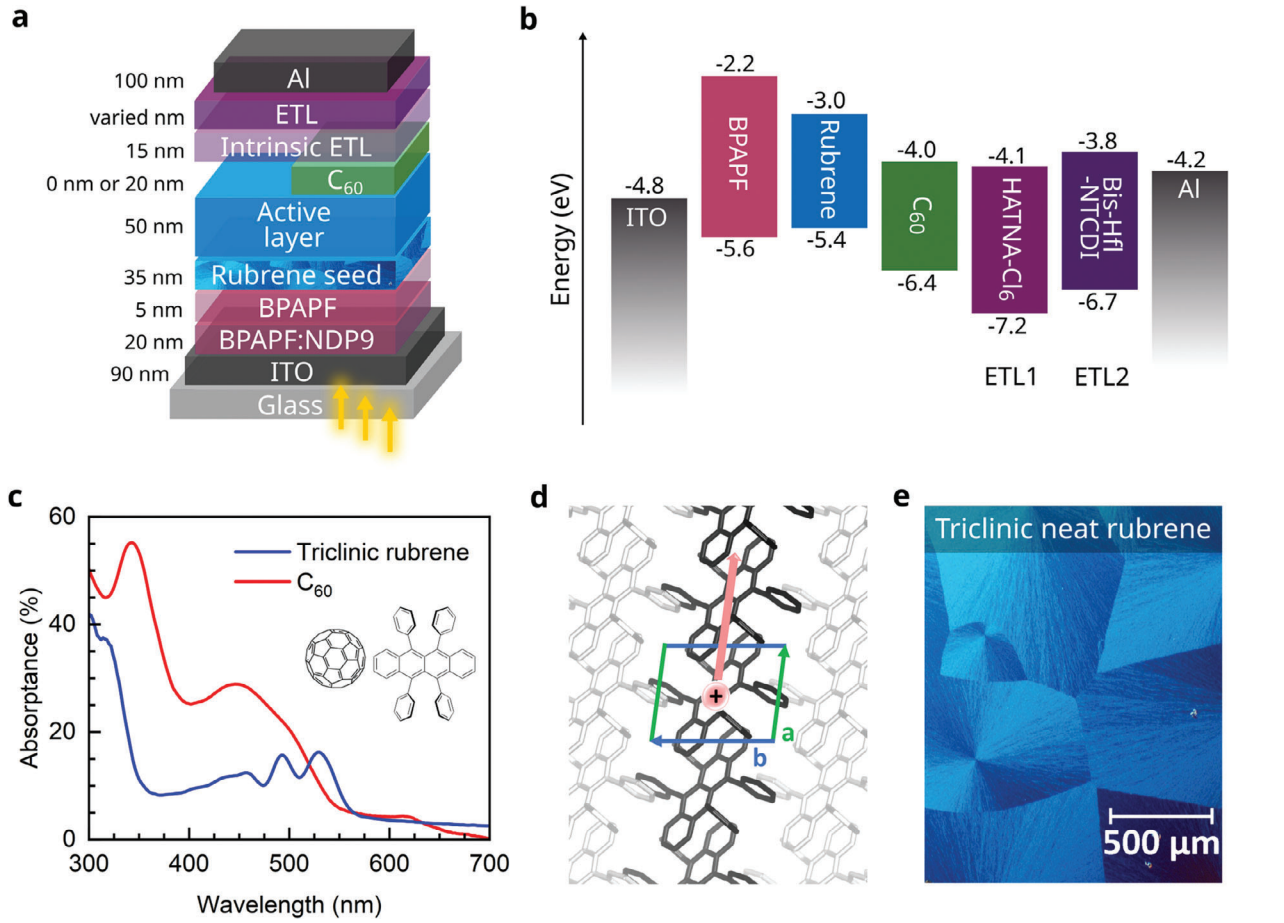

Figure 1. a) OPD device stack with bottom illumination and fixed layout for the first four layers: ITO (90 nm) / BPAPF:NDP9 (5 wt.%, 20 nm) / BPAPF (5 nm) / seed layer rubrene (35 nm). b) Energy levels of the respective materials used in the devices.[39–43] c) Absorptance of triclinic rubrene (40 nm) and C_{60} (30 nm) on a quartz glass substrate and the corresponding molecular structures. d) Triclinic unit cell along the *a*- and *b*-axis with the arrow indicating the π-stacking. e) Polarized light microscope picture of the triclinic phase.

current density of 2.5×10^{-10} A cm^{-2} at −0.1 V bias and a specific detectivity of 6×10^{11} Jones at zero bias based on the measured noise spectral density. The effects of the suppression layer and the other approaches on the roughness and crystallinity are comprehensively investigated with atomic force microscopy (AFM) and grazing-incidence wide-angle X-ray scattering (GIWAXS). This reveals a roughness on the suppression layer of only one nanometer while preserving the triclinic structure in the rubrene layer. After smoothing the triclinic layer in a thin film, it can be applied for several device concepts and is thus interesting for commercial application. Compared to studies on single crystals and lateral structures, we propel future work on vertical structures with smooth crystalline thin films. Furthermore, our strategies can be potentially applied to other material systems as well, where highly ordered films shall be used in vertical structures.

2. Results

2.1. Introduction of Material System and Stack Architecture

We decided on crystalline, triclinic rubrene as the active layer since it promotes high hole mobility in the vertical direction and is optically active. In Figure 1a, the basic stack is shown, built of ITO (90 nm) / BPAPF:NDP9 (5 wt.%, 20 nm) / BPAPF (5 nm) / seed layer rubrene (35 nm) (annealed at 140 °C) / homoepitaxially grown rubrene (50 nm) / intrinsic electron transport layer (ETL) (15 nm) / ETL:W_2(hpp)$_4$ (3 wt.%, 20 nm) / Al (100 nm). As an alternative to HATNA-Cl_6, Bis-Hfl-NTCDI is utilized as the electron transport layer (ETL) with different thicknesses. HATNA-Cl_6 and Bis-Hfl-NTCDI will be labeled as ETL1 and ETL2, respectively, throughout the work. In some cases, C_{60} is introduced as an acceptor between the active layer and ETL to achieve a donor-acceptor heterojunction. C_{60} has been used successfully with rubrene for OPDs, but so far only employing the amorphous rubrene phase.[6,44] The broad absorption of C_{60} peaks around 450 nm, while triclinic rubrene shows three distinct peaks at 460, 490, and 530 nm (Figure 1c). The triclinic unit cell of rubrene (5,6,11,12-Tetraphenyltetracen) is depicted in Figure 1d along the *a*- and *b*-axis. In the triclinic phase, rubrene arranges its tetracene core and the four attached phenyl rings such that the *a*-axis manifests as the shortest dimension. After the evaporation of a 35 nm thick seed layer on top of the hole transport layer, the film is annealed for 15 min at 140 °C in an N_2-filled glovebox with an overpressure of 3 to 4 mbar to grow the triclinic phase of rubrene (see

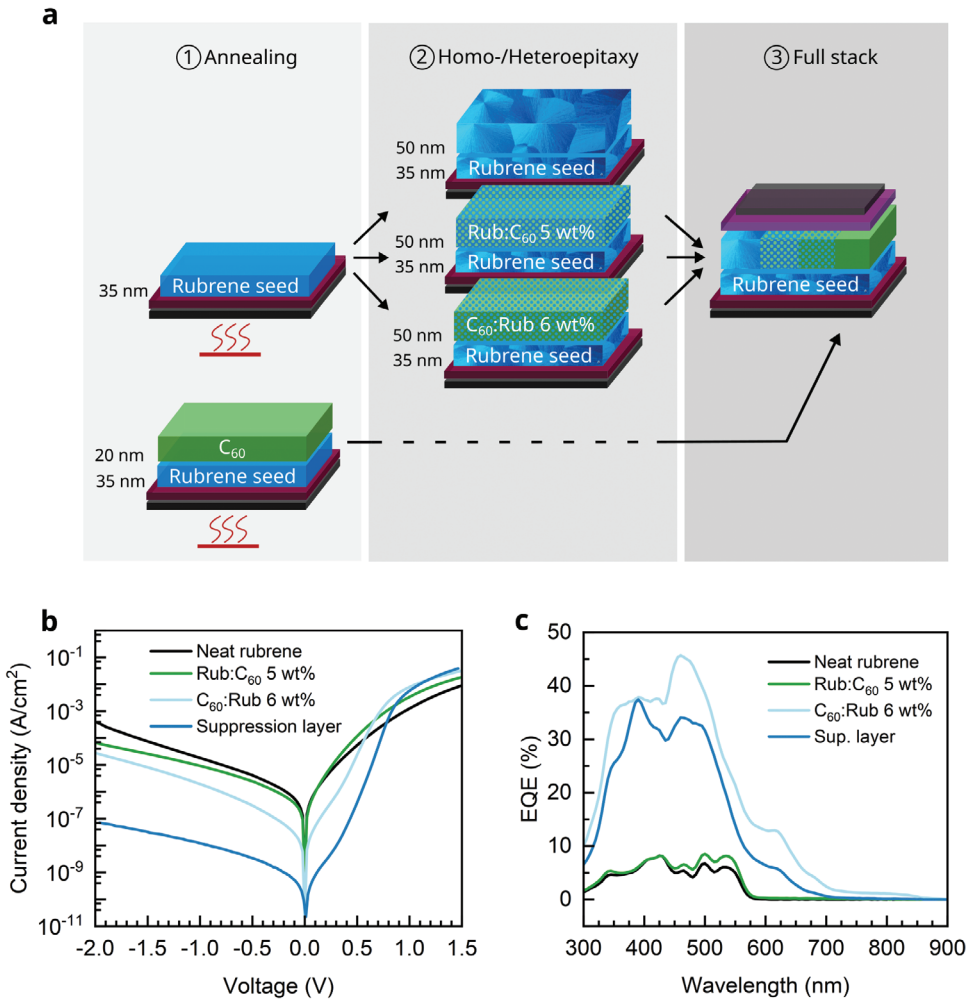

Figure 2. a) Visualization of different strategies to reduce the high dark current of OPDs based on neat triclinic rubrene active layers. On the bottom are the glass/ITO substrate in black and the HTL layers summarized in burgundy. One approach to reduce the dark current is the evaporation of different homo-/heteroepitaxy layers in the second step. These are either rubrene with 5 wt.% of C_{60} or C_{60} with 6 wt.% of rubrene. Another strategy is a C_{60} suppression layer, which is annealed together with rubrene in the first step. To complete the OPD structure, ETLs (purple) and the top electrode, aluminum (grey) are evaporated in the third step. b) Dark current density of devices with different active layers, but otherwise the same stack with ETL1 (15 nm) / ETL1:$W_2(hpp)_4$ (3 wt.%, 20 nm) as ETL. c) EQE spectra of the same devices measured at zero bias.

Figure 2a). The different triclinic orientations within a grain can be easily distinguished using polarized light microscopy due to the birefringent nature of the crystals. As shown in Figure 1e, the crystalline domains can develop up to 1 mm in diameter in the horizontal plane. For OPD devices, however, the vertical direction is most important for transport. As the seed layer has a thickness of only 35 nm, only one crystalline domain is likely formed in this direction. Additionally, 50 nm of rubrene is homoepitaxially grown on top to attain a thicker active layer for enhanced absorption; see Figure 2a. However, the surface roughness of the 35 nm thick neat triclinic seed layer is already much higher as compared to the neat amorphous, see **Figure** 3a,b. While the amorphous phase (Figure 3a) of rubrene shows an RMS (root mean square) roughness of only 0.3 nm, the triclinic phase (Figure 3b) exhibits an RMS ≈34 nm. The high roughness continues from the seed layer into the homoepitaxial layer, regardless of the active layer thickness. The RMS roughness of different homoepitaxial layer thicknesses is shown in Figure S1 (Supporting Information). The high roughness increases the probability of forming shunts in the device, significantly increasing the dark current in neat triclinic rubrene diodes (see Figure 2b). This compromises the device's performance by reducing the specific detectivity (D^*). Therefore, solutions must be found to reduce or circumvent the high surface roughness of triclinic rubrene.

2.2. Triclinic Rubrene Exhibits High Surface Roughness

The prepared standard OPD stack, containing an 85 nm triclinic neat layer of rubrene, exhibits a high dark current density of 5.7×10^{-7} A cm^{-2} at −0.1 V bias (Figure 2b), detrimental to the performance of an OPD. When comparing the AFM image of amorphous rubrene with the triclinic one in Figure 3a,b, it becomes apparent that the triclinic phase with its dendritic growth is much rougher. While the amorphous phase is very smooth with an RMS value of 0.3 nm, the triclinic phase shows an RMS

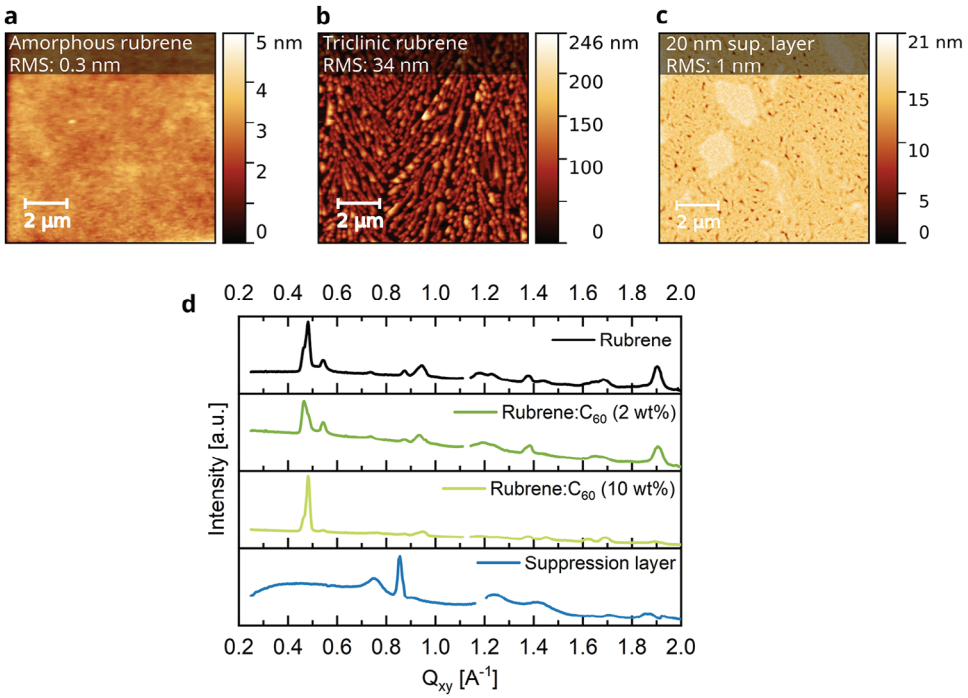

Figure 3. AFM images of 35 nm seed layer on glass of a) amorphous, b) triclinic rubrene, and c) 40 nm rubrene, which has been annealed together with C_{60} (glass / 40 nm rubrene / 20 nm C_{60}). The RMS value refers to the whole measured area. d) In-plane intensity profile of the GIWAXS data extracted for neat triclinic rubrene, 2 wt.% C_{60} and 10 wt.% C_{60} grown with 100 nm on top of the 35 nm seed layer; extracted from Figure S3 (Supporting Information). The same in-plane profile is shown for the suppression layer sample with 40 nm of rubrene suppressed by 20 nm of C_{60}, which have been annealed together; extracted from Figure S5c (Supporting Information).

roughness of 34 nm, by sampling an area of 10 × 10 µm. Even more concerning is the high peak-to-valley value of around 250 nm, more than three times the nominal thickness of the active layer. These spikes in the morphology of triclinic rubrene significantly reduce the shunt resistance in the vertical device. The ETL with 35 nm thickness is insufficient to compensate for the high roughness. Even on top of the top electrode (100 nm aluminum), an RMS roughness of 20 nm is still obtained (see Figure S1d, Supporting Information). The roughness for the rubrene template layer is also evident in GIWAXS data (Figure S4, Supporting Information) while using different incident angles. Here, we investigated a 20 nm C_{60} film on top of a pre-crystallized 35 nm triclinic rubrene template. Already for a very shallow angle of 0.08°, at which only the topmost layer, in this case C_{60}, should be probed by the X-rays for a smooth surface, the rubrene signal next to the C_{60} rings is strong. When increasing the incident angle to 0.16°, the distribution of the intensity hardly changes, suggesting that the layers are intertwined and not strictly separated in the vertical direction.

To circumvent the high roughness while still benefiting from the crystalline rubrene film, different strategies are investigated which employ homo- and heteroepitaxy of different active layers on top of the seed. In addition to neat rubrene, rubrene with 5 wt.% C_{60} and C_{60} with 6 wt.% of rubrene are examined. A different approach to reduce the surface roughness of the seed layer directly is the evaporation of a 20 nm C_{60} suppression layer right on the amorphous rubrene, which is then heated together with the rubrene layer underneath, as sketched in Figure 2a.

2.3. Strategies to Circumvent the Surface Roughness for Improving the OPD Performance

The triclinic phase exhibits deep valleys in between the single dendrites, as visible in the AFM images (Figure 3b). Moreover, scanning electron microscopy (SEM) reveals distinct voids between the dendrites in the top view (Figure S2, Supporting Information). The cross-section underlines additionally the high roughness present, with upwards-facing facets with a certain angle to the substrate. To smooth the surface by filling the voids or to reduce the roughness itself, C_{60} is incorporated with 5 wt.% in the rubrene epitaxial layer.

The RMS roughness of a homoepitaxial layer containing 5 wt.% of C_{60} is 35 nm (Figure S7a, Supporting Information), which is similar to the neat triclinic rubrene, while also the highest peak values are in the same range. OPDs with this modified active layer exhibit dark current densities in the same order of magnitude as for the neat rubrene device with 3.8×10^{-7} A cm^{-2} at −0.1 V bias (see Figure 2b). The crystallization of the homoepitaxially grown rubrene itself is not influenced by the low content of C_{60} molecules as GIWAXS measurements confirm. Due to the polycrystalline nature of the triclinic thin film, the GIWAXS data of the neat rubrene film shows multiple smeared-out peaks in the in-plane and out-of-plane directions (Figure S3a, Supporting Information). For the comparison of the neat homoepitaxially grown film and the influence of C_{60}, a low content of 2 wt.% and a higher content of 10 wt.% C_{60} are investigated. For better comparison, the in-plane profile is extracted for each sample (Figure 3d). The peak positions continue to be the same upon

doping with C_{60}, indicating that the unit cell remains constant. This is clearly shown for the most prominent peak of all configurations of the (0-11) plane in the radial direction from the origin in Figure S3d (Supporting Information). The peak width does not change upon doping with C_{60}, which confirms that C_{60} does not influence the size of the crystallites (Figure S3d, Supporting Information). However, with higher C_{60} content the amorphous background becomes more present in the GIWAXS signal (Figure S3a–c, Supporting Information). Since no C_{60} signal itself is present and it is unlikely that C_{60} is incorporated into the triclinic structure of rubrene, C_{60} presumably forms an amorphous phase with part of the rubrene. This means that the crystallization of rubrene is partly hindered by the implementation of C_{60}, and therefore, the amorphous background is increased. If there are crystalline phases of C_{60} present, the signal is most likely too weak in contrast to rubrene because of the small amount of C_{60} present in the film.

In our second approach, we use a heteroepitaxial layer of C_{60} with only 6 wt.% of rubrene, as depicted in the second panel in Figure 2a. This creates a heterojunction between rubrene and C_{60}, promoting efficient charge separation and enhancing the overall absorption of the active layer. The external quantum efficiency (*EQE*) at zero bias is enhanced to over 45%, while the samples with predominately rubrene are limited to 10% (Figure 2c). The distinct rubrene peaks are superimposed by the broad C_{60} absorption. Regarding the surface roughness, the heteroepitaxial layer of C_{60} with 6 wt.% rubrene is with an RMS roughness of 34 nm in the same range as the homoepitaxial layer with 5 wt.% C_{60} in rubrene. As shown in Figure S7b (Supporting Information), the dendrites are still visible in the AFM measurement and preserve the high roughness. Surprisingly, the C_{60} does not fill the voids but rather continues growing based on the rubrene pattern. However, for the comparison of the RMS roughness values between different samples, it has to be considered that the template layer is always different. Therefore, differences of a few nm need to be interpreted carefully.

Even though the topography is similar between the homoepitaxial layer with 5 wt.% C_{60} and the heteroepitaxial layer of C_{60} with 6 wt.% rubrene, we observe in the C_{60}-rich device a reduced dark current density of 2.8×10^{-8} A cm^{-2} at −0.1 V bias. This value is one order of magnitude lower than the homoepitaxially grown device. The reduction in dark current might be caused by the more efficient charge-transfer states formed between rubrene and C_{60} for the heteroepitaxial layer instead of the CT states between rubrene and the electron transport layer (ETL1).

While the previous two attempts of different homoepitaxy or heteroepitaxy layers failed to significantly reduce the thin film roughness, a suppression layer approach is investigated as a third solution to decrease the high roughness of the triclinic rubrene phase. As sketched in Figure 2a, a 20 nm thick layer of C_{60} is annealed together with the 35 nm seed layer of rubrene underneath to suppress the rising of high spikes in the vertical direction. The *EQE*, shown in Figure 2c, remains high with the present rubrene C_{60} heterojunction, although it is a little bit lower than for the device with C_{60} and 6 wt.% rubrene in the active layer which exhibits an intermixing of both phases. In the AFM image in Figure 3c, peak-to-valley values of only up to 21 nm are present leading to a smooth surface with an RMS roughness of only 1 nm. The dendritic growth pattern is no longer observed, as is the case for the C_{60}:Rubrene 6 wt.% sample, whereas worm-like structures are present at the surface of C_{60} with smooth islands in between. However, the different crystalline grains are clearly visible under the polarized microscope when looking at the full stack in Figure S8 (Supporting Information). Moreover, GIWAXS measurements at various incident angles, shown in Figure S5 (Supporting Information), prove that the rubrene layer underneath the C_{60} is crystalline. For a grazing incidence angle of 0.08° no distinct signal is present, while for 0.12°, the signal of the upper layer, the rings of the cubic crystal system of C_{60} become apparent. The unit cell parameter is 14.1 Å in this case when C_{60} is not constrained by the rubrene template layer. This is in good agreement with the lattice constant reported for C_{60} thin films grown on glass in the literature.[45] The signal of the triclinic phase of rubrene is not present yet for these shallow incident angles, unlike for the rough rubrene layer with C_{60} grown on top, as depicted in Figure S4 (Supporting Information). For the suppression layer, diffraction patterns of the rubrene are first visible for an incident angle of 0.16°, which demonstrates the crystallinity in the triclinic phase and the well-separated layers due to the smooth layers starting from the seed layer. The concept of a suppression layer with a low roughness while preserving the crystallinity proves successful even for smaller thicknesses of C_{60} like 5 nm or 10 nm, as can be observed in Figures S6 and S7c,d (Supporting Information). However, it becomes particularly conspicuous in the in-plane profile in Figure 3d in comparison to neat rubrene that the orientation of the crystallites is influenced by the C_{60} suppression layer. Moreover, there appears to be a subtle alteration in the unit cell. Nevertheless, the impact of the smooth active layer on the dark current in the device is distinct with a reduced dark current density of 5.7×10^{-10} A cm^{-2} at −0.1 V bias, which is three orders of magnitude smaller than in the initial neat triclinic rubrene OPD.

2.4. Further Optimizing the Device Structure

Another strategy, besides different active layers for reducing the dark current, is optimizing the heterojunction at the acceptor side and improving the energetics at the contact. We already demonstrated that it has a beneficial impact to introduce an acceptor material like C_{60} with only 6 wt.% of rubrene. Here, a 20 nm neat layer of C_{60} is applied on top of the 85 nm neat rubrene active layer, as depicted in Figure 1a). By adding this layer, the dark current density can be likewise reduced by about one order of magnitude to 4.4×10^{-8} A cm^{-2} at −0.1 V bias. In Figure S10e (Supporting Information) the improvement in dark current between the neat layer and the neat layer with additional C_{60} is shown. When 20 nm C_{60} is grown on top of a 35 nm triclinic rubrene template layer, we see an increase in the unit cell parameters to 14.4 Å compared to the 14.1 Å reported in the literature for thin films of C_{60}[45] (Figure S4a, Supporting Information), which is most likely caused by the crystalline structure of the underlying rubrene. Additionally, we increased the thickness of the ETL1 to 40 nm intending to further smooth the rough layer of the neat rubrene underneath. The impact of a thicker ETL1 layer is almost negligible. This observation is well in line with our earlier findings for the different thicknesses of the homoepitaxy with rubrene and the heteroepitaxy with C_{60} in Figures S1 and S7b (Supporting

Information). Furthermore, we tried another ETL, Bis-Hfl-NTCDI (ETL2) with different thicknesses. The opposite trend can be observed here in terms of thickness, as ETL2 also grows in a rough film. A thinner ETL2 layer lowers the dark current (see Figure S10c, Supporting Information). Overall, ETL2 is performing better than ETL1 in the device. With an ultimate thickness of 20 nm ETL2, a dark current density of 1.5×10^{-9} A cm^{-2} at −0.1 V bias is achieved for the neat rubrene OPD without our smoothing approaches (Figure S10c, Supporting Information). We also investigate the impact of the improved ETL strategy on the suppression layer, which is already smooth. With an additional C_{60} layer on top of the suppression layer and the subsequent variation of ETL1 20 and 40 nm and ETL2 50 and 100 nm, all of these latter four devices exhibit a dark current density in the low 10^{-9} A cm^{-2} region at −0.1 V bias. Therefore, the influence of the ETL material and its thickness is rather small compared to the neat rubrene device since the active layer is already smooth. Nevertheless, the optimized neat rubrene device with additional C_{60} and 20 nm ETL2 (device structure in Figure 1) can achieve a comparable dark current. However, the best performance is obtained for the suppression layer with 20 nm ETL2, but here without an additional C_{60} layer on top of the C_{60} suppression layer (device structure in Figure 2a). For this device stack, we can push the dark current one order of magnitude even further down to an ultimate dark current density of 2.5×10^{-10} A cm^{-2} at −0.1 V bias.

2.5. Comprehensive OPD Characterization

In the previous section, we successfully reduced the dark current of the OPDs by decreasing the surface roughness of the neat rubrene seed layer. We attribute this significant improvement mainly to the increased shunt resistance. In the next step, we varied the ETL layer thickness and material and were able to improve the energetics at the contact and further decrease our device's dark current. For the device with a suppression layer, we achieve a dark current density of 2.5×10^{-10} A cm^{-2} at −0.1 V bias which fits well with the trend reported by Sandberg et al.[46] and indicates that our OPD is already well-optimized in terms of shunt resistance. Furthermore, the good agreement also suggests that the dark current in our OPD is dominated by mid-gap trap states. Now, we discuss the OPD performance in more detail. Therefore, we compare our reference device (with neat triclinic rubrene in the active layer) with the devices utilizing a suppression layer with the two different ETL materials. The *EQE* spectra and *JV*-characteristics in darkness and under illumination of the other stack configurations are shown in the Supplementary Information (Figure S10, Supporting Information).

Figure 4a represents the external quantum efficiency (*EQE*) spectra measured at 0 V. For all devices, they nicely reflect the characteristic absorption peaks of rubrene at 465 and 500 nm. The absorption peak at 530 nm is less pronounced for the devices embedding C_{60}, which we attribute to the spectral overlap of the rubrene and C_{60} absorption. The C_{60} in the active layer also causes the absorption shoulder around 620 nm which is in good agreement with the absorption measurements (Figure 1c). The additional peak around 400 nm is caused by optical thin film effects as optical simulations in Figure S11c (Supporting Information) confirm. Generally, the incorporation of C_{60} in the active layer increases the *EQE* values by a factor of four due to significantly higher internal quantum efficiency (*IQE*), indicating an improved charge separation and extraction. In Figure S11d (Supporting Information), we estimated the *IQE* from the simulated absorption in the active layer embedded in the full device, and the *EQE* spectra measured at zero bias. Note that the *IQE* of more than 80% is even three times higher for the OPD with the suppression layer compared to neat triclinic rubrene due to a thinner active layer. The trend in the *EQE* is also reflected in the photocurrent measured under 100 mW cm^{-2} illumination (see Figure 4a). We attribute this improved charge generation to the creation of a donor-acceptor heterojunction between rubrene and C_{60} which enables the formation of charge-transfer (CT) states. To resolve these CT states, sensitive *EQE* (*sEQE*) measurements are conducted, and the CT state feature is fitted by a Gaussian function (see Figure S12a and Table S2, Supporting Information). Surprisingly, we obtain similar CT state energies in the range of 1.42 to 1.53 eV for all devices, even in the absence of C_{60}. We hypothesize that CT states are also formed at the planar heterojunction between rubrene and the ETL due to similar *LUMO* levels of C_{60}, ETL1, and ETL2 (cf. Figure 1b). Furthermore, the open-circuit voltage (V_{OC}) is increased to 0.82 V for the devices with a suppression layer, also exceeding the values of the OPDs containing a homo- or heteroepitaxially grown active layer (see Figure S9, Supporting Information). Since we obtain similar CT state energies for all devices, we conclude that the non-radiative voltage losses are reduced for the devices containing C_{60}, and especially for those utilizing a suppression layer. In summary, in the presence of C_{60}, we observe significantly higher *IQE* and V_{OC} related to reduced non-radiative voltage losses, such that the formation of CT states is more efficient in the C_{60} case. We also measured the *EQE* spectra at a reverse bias (see Figure S13a–c, Supporting Information). They show the same spectral shape and only a slight EQE increase by factors of 1.2 (sup. layer) and 1.5 (neat rubrene) over the whole visible spectrum with higher reverse bias, indicating efficient charge extraction already at zero bias.

The observed trend of the dark current is confirmed by measurements of the noise spectral density at a reverse bias of −2 V (see Figure 4a). While all devices show a clear $1/f$ dependence, the absolute values are shifted downwards by two orders of magnitude for the device with suppression layer and ETL2. This trend is less pronounced in the self-driven mode at zero bias as shown in Figure S14a (Supporting Information). We point out that the measured noise spectral density deviates from the estimated shot noise density by more than one order of magnitude due to the strong $1/f$ contribution at our considered operation frequency of 172 Hz. For higher frequencies, the measured noise spectral density approaches values close to the estimated shot noise level, confirming it as the dominant noise source in the devices at reverse biases and high frequencies.

Consequently, we calculated the specific detectivities D^* according to Equation (1) at the different biases based on the measured noise spectral density I_{Noise} (see Figure S15a–c, Supporting Information).

$$D^*(f, V) = EQE(f, V) \cdot e \cdot \frac{\lambda}{hc} \cdot \frac{\sqrt{A\Delta f}}{I_{Noise}(f, V)} \quad (1)$$

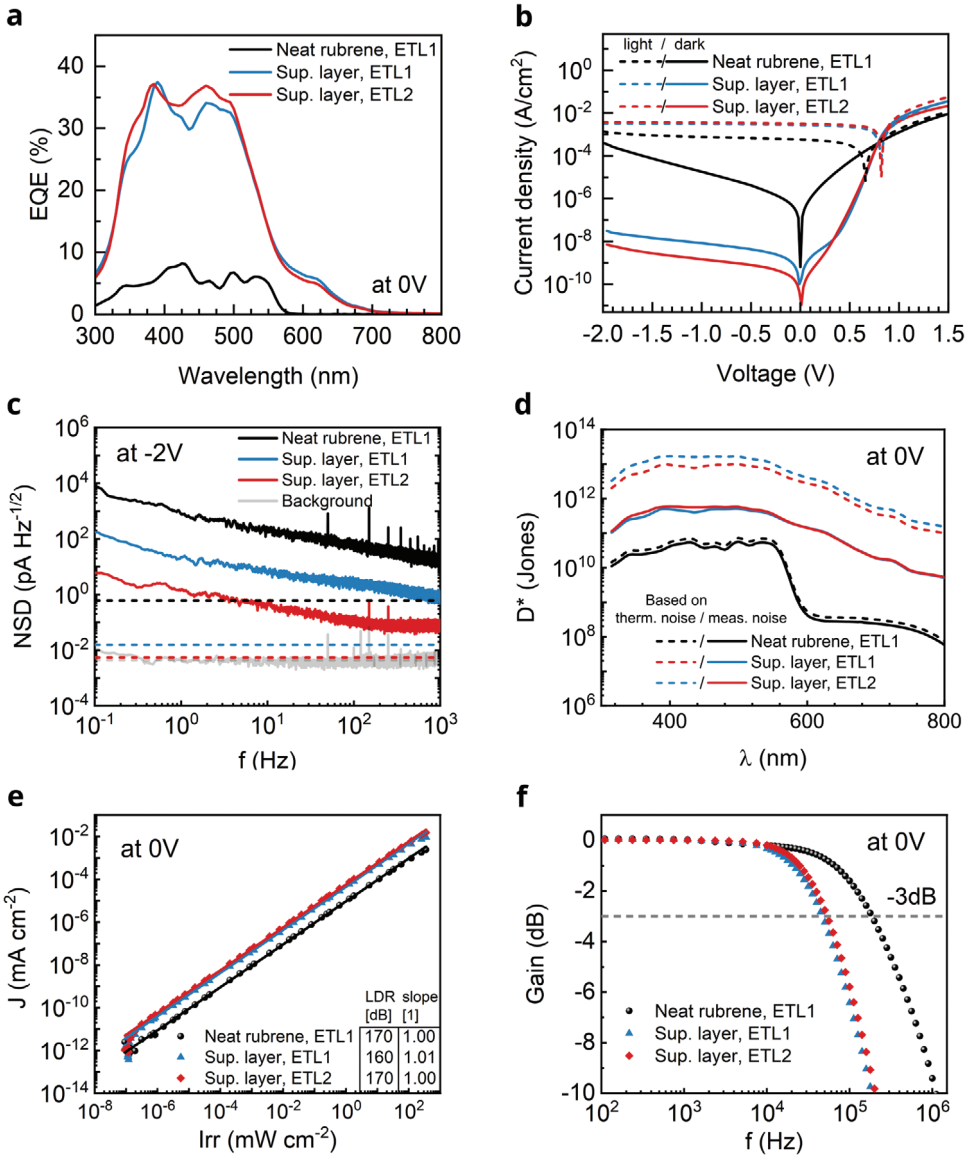

Figure 4. OPD characteristics for neat triclinic rubrene (black), triclinic rubrene with suppression layer with ETL1 (blue), and triclinic rubrene with suppression layer with ETL2 (red) in the active layer. a) EQE spectra without reverse bias and measured at 172 Hz. b) JV-characteristics under 100 mW cm^{-2} white light illumination (solid lines) and in darkness (dashed lines). c) Noise spectral densities measured at −2 V reverse bias. Dashed lines represent the calculated shot noise. d) Specific detectivity (D*) spectra measured at zero bias and 172 Hz. Solid line is calculated by considering the measured noise spectral density. Dashed line represents D* calculated based on the thermal noise. e) Linear dynamic range (LDR) measured at zero bias, 455 nm light illumination with a frequency of 172 Hz, and the solid line represents a linear fit. f) Frequency-dependent photocurrent measured at zero bias and 455 nm light with ca. 20 mW cm^{-2} irradiance.

with the frequency f and applied bias V at which EQE and I_{Noise} are measured, the elementary charge e, Planck constant h, light speed c, detector area A, and the electrical bandwidth $\Delta f = 1$ Hz. We conclude that the most sensitive operation regime for our OPDs is at zero bias with D^* achieving 6×10^{11} Jones for the device with a suppression layer and 20 nm ETL2 (see Figure 4d). Hence, we report the linear dynamic range (LDR) and the photoresponse speed at zero bias, too (see Figure 4e,f). All OPDs show photocurrent responses that are linear for a wide range of light intensities, with values of up to 170 dB. We expect that the linear photoresponses of our devices extend further for smaller light intensities, resulting in even higher LDR values. However, as we already pointed out elsewhere,[6] for weak light intensities, the measurable photocurrent is limited by the noise floor of our setup. In agreement with the EQE spectra and illuminated JV-characteristics, the photocurrent of the neat triclinic rubrene device is about a factor of four lower over the full range of investigated light intensities. A slope of unity in the double logarithmic plot is obtained for all three OPDs, indicative of negligible bimolecular recombination losses and efficient charge generation and extraction at zero bias. To measure the frequency response of the devices, we illuminate the sample with an LED of 455 nm

and an irradiance of ca. 20 mW cm^{-2}. Surprisingly, the −3 dB cutoff frequency is below 200 kHz for all devices. We hypothesize that the photoresponse speed of our devices is limited by the unbalanced mobilities of electrons and holes and is mainly governed by the lower electron mobility. We rule out *RC* limitations for the measured cutoff frequencies of our OPDs. Further, we observe a significantly higher cutoff frequency for the device with a neat triclinic rubrene active layer. We suspect that the suppression layer hinders the charge transport due to the slightly altered crystal growth of the triclinic rubrene. The rise and fall times obtained from transient photocurrent measurements are in the range of a few microseconds (see Figure S16a, Supporting Information). Further, we estimate the cutoff frequency by the following relation:[8]

$$f_{-3\mathrm{dB}} = \frac{3.5}{2\pi\, t_{\mathrm{tr}}} \tag{2}$$

where we adopt the transient time of the charge carriers (t_{tr}) with the rise time. The estimated values only slightly exceed the directly determined cutoff frequencies (see Table S2, Supporting Information) which confirms that the transit limit is dominating the photoresponse speed of our OPDs. We also studied the transient photoresponse at 20 mHz and observed excellent stability of the photocurrent generated by the OPDs (see Figure S16b, Supporting Information).

Overall, we realized sensitive organic photodetectors that utilize a crystalline rubrene layer as the photoactive material. By controlling the morphology of our active layer, we are able to increase the shunt resistance and consequently decrease the dark current by three orders of magnitude. This allows us to improve the specific detectivity by one order of magnitude and the optimized OPDs achieve 6×10^{11} Jones (based on noise measurements). Typically, specific detectivities of OPDs are reported in thermal or shot noise limit. By assuming the thermal noise limit, the specific detectivity of our OPDs is calculated to be 2×10^{13} Jones at 500 nm, competing with state-of-the-art OPDs.[8] Furthermore, our OPDs reach high *LDR* values of 170 dB, again comparable with recent OPD performance.[6] However, further device optimizations are necessary for a potential application, especially regarding the photoresponse speed. More investigations are needed to explore the origin of the comparable slow response times in the microsecond range. Finally, we want to emphasize the achieved improvements of the active layer morphology, paving the way for the application of crystalline thin films, such as in organic transistors,[37] OLEDs,[6] etc.

3. Conclusion

In summary, we investigate approaches to employ highly ordered rubrene stacks for organic photodetectors. We find a high surface roughness in the neat triclinic thin film compared to the amorphous film with peak-to-valley values of around 250 nm, detrimental to the dark current. By introducing C_{60} with 5 wt.% into the neat rubrene adlayer, using a C_{60}-rich layer on top of the seed layer, and even by adding another C_{60} layer on top of the active layer, only minor improvements in the roughness are achieved, and thus, rather large dark currents are observed. Instead, by controlling the rubrene morphology with a 20 nm C_{60} suppression layer, we are able to smoothen the rubrene thin film to an RMS roughness of only 1 nm while still preserving the triclinic structure. We confirm the crystallinity with GIWAXS measurements by accessing different layers with several incident angles, where we find slightly different lattice parameters for the triclinic unit cell. After the optimization of the ETL material to Bis-HFl-NTCDI (ETL2) and its thickness to 20 nm, we demonstrate with the strategy of a suppression layer a crystalline OPD with three orders of magnitude lower dark current, which is 2.5×10^{-10} A cm^{-2} at −0.1 V bias. We attribute this reduction in dark current to an increased shunt resistance compared to the initial rough, neat triclinic rubrene layer. With the incorporation of C_{60} for the suppression layer, we further improved the *EQE* to over 35 % at zero bias due to better charge separation and extraction. The lower noise spectral density in the optimized smooth device and the good *EQE* lead to a specific detectivity D^* of 6×10^{11} Jones (based on noise measurement) and a high *LDR* value of 170 dB at zero bias. Utilizing a suppression layer in our strategy has demonstrated notable success, showing great potential for application in various other crystalline organic semiconductors.

4. Experimental Section

Materials and Substrates: The glass substrates were purchased from Thin Film Devices TFD Inc., USA with ≈ 90 nm of prestructured ITO. 9,9-bis[4-(N,N-bis-biphenyl-4-yl-amino)phenyl]−9H-fluorene (BPAPF) and 2,3,8,9,14,15-hexachloro-5,6,11,12,17,18-hexaazatrinaphthylene (HATNA-Cl_6) was purchased from Luminescence Technology Corp., Taiwan. NDP9 was purchased from Novaled GmbH, Germany. Rubrene is from TCI Deutschland GmbH, while C_{60} and N,N-Bis(fluoren-2-yl)-naphthalenetetracarboxylic diimide (Bis-HFl-NTCDI) are purchased from CreaPhys GmbH, Germany. Tetrakis(1,3,4,6,7,8-hexahydro-2H-pyrimido[1,2-a]pyrimidinato)ditungsten (II) ($W_2(hpp)_4$) was synthesized in house. Aluminum (Al) was purchased from Kurt J. Lesker, USA. All organic materials are sublimed at least one time before use.

Device Preparation: All of the devices were thermally evaporated in a multi-source vacuum chamber system (Kurt J. Lesker, UK) with a base pressure of less than 10^{-7} mbar. The prestructured ITO substrates were cleaned beforehand with the following procedure: They are placed in an ultrasonic bath in a dimethyl sulfoxide (DMSO) solution for 20 min. Afterward, they are rinsed for 5 min with DI water and then placed again in the ultrasonic bath for 10 min with DI water and subsequently with ethanol for 10 min. The samples are placed in a spin-rinser-dryer for another 10 min. The last step is a plasma treatment for 10 min. For the doped layers the density of the dopant was assumed to be the same as the matrix material. Shadow masks were used to achieve the device structure. The geometric overlap of the bottom and the top contact is taken as active area of the pixel to 6.44 mm^2. All devices were encapsulated by gluing transparent glass with a UV-cured epoxy resin (Nagase ChemteX XNR 5592, Japan) on top of the device after fabrication. Beforehand a moisture getter (Dynic Ltd., UK) is inserted into a cavity in the cover glass to prevent device 0 degradation.

UV-VIS Absorption: Reflection and transmittance spectra were acquired in an integrating sphere with a laboratory UV-VIS-NIR spectrometer (Shimadzu SolidSpec-3700, Japan). Subsequently, the absorptance was calculated via $A = 1 - T - R$. The neat films were measured on a glass substrate.

Ellipsometry: Spectroscopic ellipsometry data (M2000-VI, J. A. Woollam Co. Inc; wavelength: 245–1700 nm, angles of incidence: 55°–75°) was modeled to derive optical constants of triclinic rubrene films annealed together with 1) and without 2) a 20 nm C_{60} top layer. In case 1), a two-layer-model with a uniaxial bottom rubrene layer (1 Tauc-Lorentz and 5 Gaussian oscillators, energy positions, and oscillator widths coupled, *z* to

xy) and isotropic C_{60} top layer was used. In case (2), ellipsometric data of an annealed triclinic rubrene film could not be modeled due to the high roughness of the rubrene surface. Thus, 20 nm C_{60} was deposited after annealing to reduce the surface roughness. For this layer system, a rubrene bottom layer (1 Tauc-Lorentz and 8 Gaussian oscillators, energy positions, and oscillator widths coupled, *z* to *xy*) and a 3-component effective medium top-layer (C60 (11%), triclinic rubrene (51%), and void (38%); all volume fractions fitted) were modeled. Optical constants of rubrene in the bottom and top layers were fitted individually. All substrates were 500 nm SiO_2 on Si-wafer and optical constants of the substrate materials were taken from the database (CompleteEASE). Uniaxial anisotropy of rubrene films was ensured by measurements at various in-plane rotation angles of the samples.

Polarized Light Microscopy: A Nikon ECLIPSE LV100ND microscope was used with a polarization filter to obtain the different grains of triclinic rubrene.

AFM: Atomic force microscopy was conducted with the tool from Nanosurf AG Flex-Axiom, Switzerland in tapping mode and post-processed with Gwyddion.

GIWAXS: The grazing-incidence wide-angle X-ray scattering (GIWAXS) experiments for the rubrene:C_{60} blends (Figure S3, Supporting Information) were performed at beamline XRD1 at ELETTRA, Italy. The beam energy was 12.4 keV, and the beam had a diameter of 200 µm. A Pilatus 2 M area detector was positioned 399.9 mm behind the sample, and the sample-to-detector distance, as well as the beam center, were verified by measuring a lanthanum hexaboride reference. The incident angle of the beam was 0.1° and the samples were exposed for 240 s to the beam while being rotated for 360°.

The incident angle-dependent experiments with rubrene/C_{60} bilayers annealed before or after C_{60} deposition (Figures S4 and S5, Supporting Information) were performed at beamline NCD-SWEET at ALBA, Spain. The beam energy was 12.4 keV, and the beam had dimensions of around 10 µm vertically and 100 µm horizontally. A Pilatus 1 M area detector was positioned 211 mm behind the sample, and the sample-to-detector distance, as well as the beam center, were verified by measuring a chromium(III) oxide reference. The samples were exposed for 5 × 5 s to the beam and the resulting images are the average of the 5 recorded images.

The experiments with the rubrene/C_{60} bilayers with different C_{60} thicknesses (Figure S6, Supporting Information) were performed at beamline XRD1 at ELETTRA, Italy. The beam energy was 12.4 keV, and the beam had a diameter of 200 µm. A Pilatus 2 M area detector was positioned 407.5 mm behind the sample, and the sample-to-detector distance, as well as the beam center, were verified by measuring a lanthanum hexaboride reference. The incident angle of the beam was 0.12°, and the samples were exposed for 60 s. All the data were analyzed by using WxDiff.

Scanning Electron Microscopy: Scanning Electron Microscopy (SEM) was conducted with a Zeiss Gemini 500 SEM operated at 4 kV and observed with a secondary-electron detector placed on the side under 10^{-5} mbar vacuum. No additional conductive coating was needed since the organic allowed for sufficient electron flow toward the silicon substrate.

Current-Voltage Characteristics: The *JV*-characteristics under illumination were measured at a light intensity of 100 mW cm^{-2} utilizing a 300 W xenon lamp (Ushio UXL-300D-0, Japan) in a sun simulator (Solar Light Co. Sunlight simulator 16S-003-300-AM1.5, USA). The light intensity was referenced to a silicon photodiode (Hamamatsu Photonics S1337, Japan) and not mismatch corrected. A source measuring unit (Keithley Instruments SMU 2400, USA) was used for the voltage-dependent current measurements under illumination. For the dark *JV*-curves, a highly sensitive measuring unit (Keithley Instruments SMU 2635A, USA) with long holding times was utilized to rule out capacitive charge effects. The setup was controlled by the measurement software SweepMe! (https://sweep-me.net).

External Quantum Efficiency: For the *EQE* measurements, a 150 W xenon lamp (Ushio UXL-150SO, Japan) was used in combination with a monochromator (Newport Cornerstone 260 1/4m, USA). The light was chopped at a frequency of 172 Hz and induced a photocurrent in the OPD which was amplified by a current-voltage preamplifier (Stanford Research SR570, USA) and afterward fed into a lock-in amplifier (Signal Recovery SR 7265, USA). The light intensity was referenced to a silicon diode (Hamamatsu Photonics S1337, Japan). Both the sample and the reference were masked to define an exact photoactive area of 2.997 mm^2.

Sensitive External Quantum Efficiency: The light of a 250 W halogen lamp (OSRAM HLX 64 657, Germany) was chopped at 172 Hz and coupled into a double monochromator (Quantum Design GmbH MSHD-300A, Germany). Afterward, the light was focused onto the OPD, and its generated photocurrent was measured under short-circuit conditions. A current-voltage preamplifier (Stanford Research Systems SR 570, USA) was used to magnify the photocurrent and subsequently provided to a lock-in amplifier (Stanford Research Systems SR830, USA). A calibrated Si and InGaAs photodiode (Thorlabs FDS100-CAL, USA and Hamamatsu Photonics G12183_020K, Japan) was used to measure the flux of incident photons. The setup was controlled by the measurement software SweepMe! (https://sweep-me.net).

Noise Spectral Density: An electrically shielded box was used to provide darkness and disentangle the real noise data from the ambient environment and electrical artifacts. By utilizing a low-noise current-voltage preamplifier (FEMTO Messtechnik GmbH DLPCA-200, Germany) the time-dependent dark current was amplified and recorded by a high-speed, low-noise oscilloscope (Tektronix DPO7354C, USA) with a sampling rate of 20 000 Sampling s^{-1}. The noise spectra were calculated from Welch's method[47] and smoothed by a Savitzky-Golay filter.

Linear Dynamic Range: The OPDs were illuminated by a 455 nm LED (Thorlabs M455L4, USA) driven by an LED driver (Mightex Systems BLS-1000-2, Canada) and modulated at 172 Hz. A series of neutral density filters (Thorlabs, USA) was utilized to achieve a wide light intensity range. The generated photocurrent of the OPD was preamplified (FEMTO Messtechnik GmbH DLPCA-200, Germany) and fed into a lock-in amplifier (Stanford Research Systems SR865A, USA). The light intensity was referenced to a silicon photodiode (Thorlabs SM05PD3A, USA). For the reduction of external noise sources, an electrically shielded box was used. The setup was controlled by the measurement software SweepMe! (https://sweep-me.net).

Transient Photocurrents: Transient photocurrents were measured under illumination with the same LED 455 nm, and the corresponding driver operated at 10 kHz or 20 mHz as mentioned above. The generated photocurrent was magnified by a fast current-voltage preamplifier (FEMTO Messtechnik GmbH DHPCA-100, Germany) and recorded by the same oscilloscope (Tektronix DPO7354C, USA) as used for the noise current measurements. Rise and fall times are calculated at 10% and 90% of the maximum photocurrent as usually reported in the literature.[48,49]

−3 dB Cutoff Frequency: An LED with an emission wavelength of 455 nm (Thorlabs M455L4, USA) and with 20 mW cm^{-2} irradiance was modulated at frequencies up to 4 MHz. The generated photocurrent of the investigated OPD was then preamplified (FEMTO Messtechnik GmbH DHPCA-100, Germany) and fed into a lock-in amplifier (Stanford Research Systems SR865A, USA). The light intensity was calibrated to a silicon photodiode (Thorlabs SM05PD3A, USA). The setup was controlled by the measurement software SweepMe! (https://sweep-me.net).

Optical Simulations: The open-source python program "Simojio" was used to run the optical simulations.[50] The software is based on the transfer matrix model (TMM), which was implemented by S. Byrnes in the python package "tmm".[51] The optical constants of the triclinic rubrene layer were obtained from modeling ellipsometry (see Figure S11a, Supporting Information). For the other materials, the values are taken from the literature.

Supporting Information

Supporting Information is available from the Wiley Online Library or from the author.

Acknowledgements

A.-L.H., J.W. contributed equally to this work. The authors acknowledge funding from the Koselleck-project (456344071) from the German

Research Foundation (DFG) and the project funding "FLEXMONIRS" (01DR20008) from the German Federal Ministry of Education and Research (BMBF). The authors acknowledge Elettra Sincrotrone Trieste for providing access to its synchrotron radiation facilities and for financial support under the IUS internal project. The authors thank Dr. Luisa Barba for assistance in using beamline XRD1. The incidence angle dependent experiments were performed at the NCD-SWEET beamline at ALBA Synchrotron with the collaboration of ALBA staff. The authors would like to thank Dr. Cristián Huck for his help in setting up the experiment. The authors thank the Dresden Center for Nanoanalysis for granting access to the SEM facility. Furthermore, the authors acknowledge Sebastian Schellhammer for fruitful discussion and for making the sketch of the triclinic unit cell in Figure 1d.

Open access funding enabled and organized by Projekt DEAL.

Conflict of Interest

K.L. is shareholder of Senorics GmbH, a manufacturer of organic photodetectors.

Data Availability Statement

The data that support the findings of this study are available from the corresponding author upon reasonable request.

Keywords

crystalline rubrene, grazing-incidence wide-angle X-ray scattering (GIWAXS), organic photodetectors, thin-films

Received: April 15, 2024
Revised: May 31, 2024
Published online: June 29, 2024

[1] Q. Lin, A. Armin, P. L. Burn, P. Meredith, *Nat. Photonics.* **2015**, *9*, 687.
[2] J. Liu, J. Jiang, S. Wang, T. Li, X. Jing, Y. Liu, Y. Wang, H. Wen, M. Yao, X. Zhan, L. Shen, *Small.* **2021**, *17*, 2101316.
[3] T. Lin, J. Wang, *Adv. Mater.* **2019**, *31*, 1901473.
[4] M. Sawatzki-Park, S. J. Wang, H. Kleemann, K. Leo, *Chem. Rev.* **2023**, *123*, 8232.
[5] Y. Wang, T. Zhang, D. Samigullina, L. C. Winkler, F. Dollinger, J. Kublitski, X. Jia, R. Ji, S. Reineke, D. Spoltore, K. Leo, J. Benduhn, *Adv. Funct. Mater.* **2024**, *34*, 2313689.
[6] T. Zhang, L. C. Winkler, J. Wolansky, J. Schröder, K. Leo, J. Benduhn, *Adv. Funct. Mater.* **2024**, *34*, 2308719.
[7] A. Armin, M. Hambsch, I. K. Kim, P. L. Burn, P. Meredith, E. B. Namdas, *Laser Photonics Rev.* **2014**, *8*, 924.
[8] Y. Wang, J. Kublitski, S. Xing, F. Dollinger, D. Spoltore, J. Benduhn, K. Leo, *Mater. Horiz.* **2022**, *9*, 220.
[9] T. Shan, X. Hou, X. Yin, X. Guo, *Front. Optoelectron.* **2022**, *15*, 49.
[10] S. Xing, J. Kublitski, C. Hänisch, L. C. Winkler, T. yi Li, H. Kleemann, J. Benduhn, K. Leo, *Adv. Sci.* **2022**, *9*, 2105113.
[11] J. Kublitski, A. Hofacker, B. K. Boroujeni, J. Benduhn, V. C. Nikolis, C. Kaiser, D. Spoltore, H. Kleemann, A. Fischer, F. Ellinger, K. Vandewal, K. Leo, *Nat. Commun.* **2021**, *12*.
[12] G. Chen, Y. Yu, Y. Shi, N. Li, W. Luo, L. Cao, A. J. Danner, A. Q. Liu, X. Zhang, *Laser Photonics Rev.* **2022**, *16*, 2200117.
[13] J. J. Ackert, D. J. Thomson, L. Shen, A. C. Peacock, P. E. Jessop, G. T. Reed, G. Z. Mashanovich, A. P. Knights, *Nat. Photonics.* **2015**, *9*, 393.
[14] S. Ullbrich, B. Siegmund, A. Mischok, A. Hofacker, J. Benduhn, D. Spoltore, K. Vandewal, *J. Phys. Chem. Lett.* **2017**, *8*, 5621.
[15] J. Zheng, D. Yang, D. Guo, L. Yang, J. Li, D. Ma, *ACS Photonics.* **2023**, *10*, 1382.
[16] W. Brütting, C. Adachi, R. J. D. Holmes, *Physics of Organic Semiconductors*, Wiley-VCH, Weinheim, Germany **2012**, p. 634.
[17] K. Miyashige, M. Morimoto, S. Naka, *Phys. Status Solidi Appl. Mater. Sci.* **2021**, *218*.
[18] H. Bässler, A. Köhler, in *InOrganic Light-Emitting Diodes (OLEDs)*, Woodhead Publishing, Sawston **2013**, pp. 192.
[19] Y. Zhang, Y. Yuan, P. Wang, H. Gao, Z. Qin, D. Liu, X. Zhang, C. Gao, H. H. Fang, W. Hu, H. Dong, *J. Phys. Chem. C.* **2024**, *128*, 3431.
[20] T. Takeda, M. Ozawa, T. Akutagawa, *Angew. Chem.* **2019**, *131*, 10453.
[21] J. Kondrasiuk, A. Szymanski, *Mol. Cryst. Liq. Cryst.* **1972**, *18*, 379.
[22] R. G. Kepler, *Phys. Rev.* **1960**, *119*, 1226.
[23] L. F. Ji, J. X. Fan, S. F. Zhang, A. M. Ren, *Phys. Chem. Chem. Phys.* **2018**, *20*, 3784.
[24] O. D. Jurchescu, J. Baas, T. T. M. Palstra, *Appl. Phys. Lett.* **2004**, *84*, 3061.
[25] J. Takeya, M. Yamagishi, Y. Tominari, R. Hirahara, Y. Nakazawa, T. Nishikawa, T. Kawase, T. Shimoda, S. Ogawa, *Appl. Phys. Lett.* **2007**, *90*, 102120.
[26] M. F. Sawatzki, H. Kleemann, B. K. Boroujeni, S. J. Wang, J. Vahland, F. Ellinger, K. Leo, *Adv. Sci.* **2021**, *8*, 2003519.
[27] T. Hasegawa, J. Takeya, *Sci. Technol. Adv. Mater.* **2009**, *10*, 024314.
[28] K. Kim, M. K. Kim, H. S. Kang, M. Y. Cho, J. Joo, J. H. Kim, K. H. Kim, C. S. Hong, D. H. Choi, *Synth. Met.* **2007**, *157*, 481.
[29] Q. Du, S. Qin, Z. Wang, Y. Gan, Y. Zhang, L. Fan, Y. Liu, S. Li, R. Dong, C. Liu, W. Wang, F. Wang, *ACS Appl. Mater. Interfaces.* **2021**, *13*, 57735.
[30] A. Li, X. Wei, Y. He, C. He, M. U. Ali, H. Yang, O. Goto, H. Meng, *Appl. Phys. Lett.* **2018**, *113*, 103301.
[31] Q. Du, Z. Wang Du, M. Li Du, Y. Gan, S. Li, Y. Liu, W. Wang, F. Wang, S. Qin, *J. Mater. Chem. C.* **2023**, *11*, 5182.
[32] S. W. Park, J. M. Hwang, J. M. Choi, D. K. Hwang, M. S. Oh, J. H. Kim, S. Im, *Appl. Phys. Lett.* **2007**, *90*, 153512.
[33] H. M. Lee, H. Moon, H. S. Kim, Y. N. Kim, S. M. Choi, S. Yoo, S. O. Cho, *Org. Electron.* **2011**, *12*, 1446.
[34] T. R. Fielitz, R. J. Holmes, *Cryst. Growth Des.* **2016**, *16*, 4720.
[35] L. Huang, Q. Liao, Q. Shi, H. Fu, J. Ma, J. Yao, *J. Mater. Chem.* **2010**, *20*, 159.
[36] J. J. Kim, H. M. Lee, J. W. Park, S. O. Cho, *J. Mater. Chem. C.* **2015**, *3*, 2650.
[37] S. J. Wang, M. Sawatzki, G. Darbandy, F. Talnack, J. Vahland, M. Malfois, A. Kloes, S. Mannsfeld, H. Kleemann, K. Leo, *Nature.* **2022**, *606*, 700.
[38] J. Euvrard, O. Gunawan, A. Kahn, B. P. Rand, *Adv. Funct. Mater.* **2022**, *32*, 2206438.
[39] L. E. Polander, P. Pahner, M. Schwarze, M. Saalfrank, C. Koerner, K. Leo, *APL Mater.* **2014**, *2*, 081503.
[40] F. Anger, T. Breuer, A. Ruff, M. Klues, A. Gerlach, R. Scholz, S. Ludwigs, G. Witte, F. Schreiber, *J. Phys. Chem. C.* **2016**, *120*, 5515.
[41] X. Zhao, T. Liu, H. Liu, S. Wang, X. Li, Y. Zhang, X. Hou, Z. Liu, W. Shi, T. J. S. Dennis, *ACS Appl. Mater. Interfaces.* **2018**, *10*, 42715.
[42] S. Barlow, Q. Zhang, B. R. Kaafarani, C. Risko, F. Amy, C. K. Chan, B. Domercq, Z. A. Starikova, M. Y. Antipin, T. V. Timofeeva, B. Kippelen, J. L. Brédas, A. Kahn, S. R. Marder, *Chem. – Eur. J.* **2007**, *13*, 3537.
[43] M. Schwarze, B. D. Naab, M. L. Tietze, R. Scholz, P. Pahner, F. Bussolotti, S. Kera, D. Kasemann, Z. Bao, K. Leo, *ACS Appl. Mater. Interfaces.* **2018**, *10*, 1340.
[44] D. Yang, X. Zhou, D. Ma, *Org. Electron.* **2013**, *14*, 3019.
[45] C. Elschner, A. A. Levin, L. Wilde, J. Grenzer, C. Schroer, K. Leo, M. Riede, *J. Appl. Crystallogr.* **2011**, *44*, 983.

[46] O. J. Sandberg, C. Kaiser, S. Zeiske, N. Zarrabi, S. Gielen, W. Maes, K. Vandewal, P. Meredith, A. Armin, *Nat. Photonics.* **2023**, *17*, 368.
[47] P. D. Welch, *IEEE Trans. Audio Electroacoustics.* **1967**, *15*.
[48] D. Yang, D. Ma, *Adv. Opt. Mater.* **2019**, *7*, 1800522.
[49] C. Fuentes-Hernandez, W.-F. Chou, T. M. Khan, L. Diniz, J. Lukens, F. A. Larrain, V. A. Rodriguez-Toro, B. Kippelen, *Science.* **2020**, *370*, 698.
[50] Simojio Simulation Tool https://github.com/simoji-dev/simojio, (accessed: April 2024).
[51] S. J. Byrnes, *arXiv.* **2016**, 160302720.